Vanadyl sulfates

Citation for published version:
Ignaszak, A, Patterson, N, Radtke, M, Elsegood, MRJ, Frese, JWA, Lipman, JLZF, Yamato, T, Sanz, S, Brechin, EK, Prior, TJ & Redshaw, C 2018, 'Vanadyl sulfates: molecular structure, magnetism and electrochemical activity', *Dalton Transactions*, vol. 47, no. 44, pp. 15983-15993. https://doi.org/10.1039/C8DT03626H

Digital Object Identifier (DOI):
10.1039/C8DT03626H

Link:
Link to publication record in Edinburgh Research Explorer

Document Version:
Peer reviewed version

Published In:
Dalton Transactions

Journal Name

ARTICLE

Vanadyl sulfates: molecular structure, magnetism and electrochemical activity

Received 00th January 20xx,
Accepted 00th January 20xx

DOI: 10.1039/x0xx00000x

www.rsc.org/

Anna Ignaszak[a *], Nigel Patterson, [a] Mariusz Radtke,[a] Mark R. J. Elsegood,[b] Josef W. A. Frese.[b] Joah L. Z. F. Lipman,[b] Takehiko Yamato,[c] Sergio Sanz,[d] Euan Brechin,[d] Timothy J. Prior[e] and Carl Redshaw[e *]

Reaction of differing amounts of vanadyl sulfate with p-*tert*-butylthiacalix[4]areneH$_4$ and base allows access to the vanadyl-sulfate species $[NEt_4]_4[(VO)_4(\mu_3\text{-}OH)_4(SO_4)_4]\cdot{}^1/_2H_2O$ (**1**), $[HNEt_3]_5[(VO)_5(\mu_3\text{-}O)_4(SO_4)_4]\cdot 4MeCN$ (**2**·4MeCN) and $[NEt_4]_2[(VO)_6(O)_2(SO_4)_4(OMe)(OH_2)]\cdot MeCN$ (**3**·MeCN). Similar use of p-*tert*-butylsulfonylcalix[4]areneH$_4$, p-*tert*-butylcalix[8]areneH$_8$ or p-*tert*-butylhexahomotrioxacalix[3]areneH$_3$ led to the isolation of [HNEt$_3$]$_2$[H$_2$NEt$_2$]$_2$[VO(OMe)]$_2$p-*tert*-butylcalix[8-SO$_2$]areneH$_2$] (**4**), [HNEt$_3$]$_2$[V(O)$_2$p-*tert*-butylcalix[8]areneH$_5$] (**5**) and $[HNEt_3]_2[V^{IV}{}_2V^{V}{}_4O_{11}(OMe)_8]$ (**6**), respectively. Dc magnetic susceptibility measurements were performed on powdered microcrystalline samples of **1**-**3** in the T = 300 - 2 K temperature range. Preliminary screening for electrochemical water oxidation revealed some activity for **2** with turnover frequency (TOF) and number (TON) of 2.2×10^{-4} s^{-1} and 6.44×10^{-6} (mmol O$_2$ / mmol cat.), respectively. The compound **3** showed an improved electrochemical activity in the presence of water. This is related to the increased number and the rate of electrons exchanged during oxidation of V^{4+} species, facilitated by protons generated in the water discharge process.

Introduction

There has been interest in the coordination chemistry of oxo vanadium species for many years given their relevance to a number of enzyme structures. For example, in the haloperoxidases, which, as the name suggests, promote halide transfer reactions, the active site has been identified as containing a mono-nuclear metal centre in the form of a vanadate.[1] Furthermore, there is a drive to model the active site of vanadium haloperoxidase enzymes.[2] Our interest in vanadyl species stems from their catalytic potential in a variety of processes, and our on-going investigations into constrained ligand-metal environments.[3]

Given our enthusiasm for metallocalixarene chemistry,[4] we were attracted to a report by Luneau *et al.* describing that, under anerobic solvothermal conditions, use of a calix[4]arene (with VOSO$_4$/base) resulted in a Lindqvist-type poly(oxo)hexavanadate possessing a $[V^{III}(V^{IV})_5O_{19}]$ core with retention of the template calixarene.[5] We note that only a limited number of vanadyl calixarenes are known, for which applications are somewhat limited (mainly oxidation of alcohols, polymerisation catalysis or as potential anti-cancer agents).[6] Thus, we sought to further exploit the Luneau methodology in order to try and access new vanadium-based species. Furthermore, Santoni, Scandola, Campagna *et al* have also highlighted the potential of polyoxovanadates to function as water oxidation catalysts.[7] In particular, the mixed-valance complex $[(V^{IV}{}_5V^{V})O_7(OMe)_{12}]^{-}$, in the presence of Ru(bipy)$_3^{2+}$ (as photosensitizer) and Na$_2$S$_2$O$_8$ (as sacrificial electron acceptor), was shown to catalyse the photoinduced oxidation of water at pH7 with a quantum yield of 0.20. This suggests that, given the diversity of polyoxovanadate clusters available, this is a fertile research area. With this in mind, we have embarked upon a programme to screen the electrocatalysis of new vanadyl-containing species. We note also that polyoxovanadates are of interest due to their attractive magnetic properties, with much of the early work reported by Klemperer *et al.*,[8] Zubieta *et al.*,[9] Hill *et al.*,[10] and Mikuriyu *et al.*,[11] whilst in more recent times the challenge has been taken up by McInnes *et al.*[12]

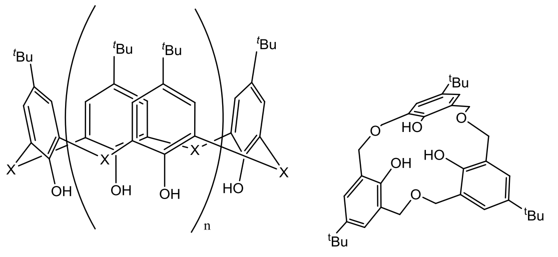

n = 1, X = S (L^{4S}H$_4$); X = SO$_2$ (L^{4SO2}H$_4$)
n = 2, X = CH$_2$ (L^{6CH2}H$_6$)
n = 3, X - CH$_2$ (L^{8CH2}H$_8$)

(L^{CH2OCH2}H$_3$)

Chart 1. Calixarene ligands used in this work

---

[a] Department of Chemistry, University of New Brunswick, Fredericton, NB, E3B 5A3, Canada. E-mail: aignasza@unb.ca.
[b] Chemistry Department, Loughborough University, Loughborough, LE11 3TU, UK.
[c] Department of Applied Chemistry, Saga University, Honjo-machi, 840-8502, Saga-shi, Japan
[d] EaStCHEM School of Chemistry, University of Edinburgh, Edinburgh, EH9 3FJ, Scotland
[e] School of Mathematics and Physical Sciences, The University of Hull, Hull, HU6 7RX, UK, E-mail: c.redshaw@hull.ac.uk

Electronic Supplementary Information (ESI) available: [Alternative views of **1** – **6**; crystallographic experimental; CV, DPE and BE scans for **2**, and CV for **5**]. See DOI: 10.1039/x0xx00000x

Herein, we report that by changing to non-solvothermal, and anerobic conditions, the Luneau reaction follows a different pathway and that the use of different calixarenes (and stoichiometries) can afford very different polyoxovanadates. We have examined the molecular structures, electrochemistry and magnetism of these species.

The calixarenes shown in chart 1 have been employed in this work, and their use led to the products **1** – **6** depicted in chart 2. Our initial studies focused on the use of p-*tert*-butylthiacalix[4]areneH$_4$, $L^{4S}H_4$, which by varying the ratio of $[L^{4S}H_4]$:[V] allows for the high yield synthesis of tetra- (**1**), penta- (**2**) or hexa-polyoxovanadates (**3**); the base employed can be either Et_3N or Et_4NOH. Extending the studies to p-*tert*-butylsulfonylcalix[4]areneH$_4$, $L^{4SO2}H_4$, p-*tert*-butylcalix[8]areneH$_8$, $L^{8CH2}H_4$, or p-*tert*-butylhexahomotrioxacalix[3]areneH$_3$, $L^{CH2OCH2}H_3$, led to the isolation of the products **4**, **5** and **6**, respectively.

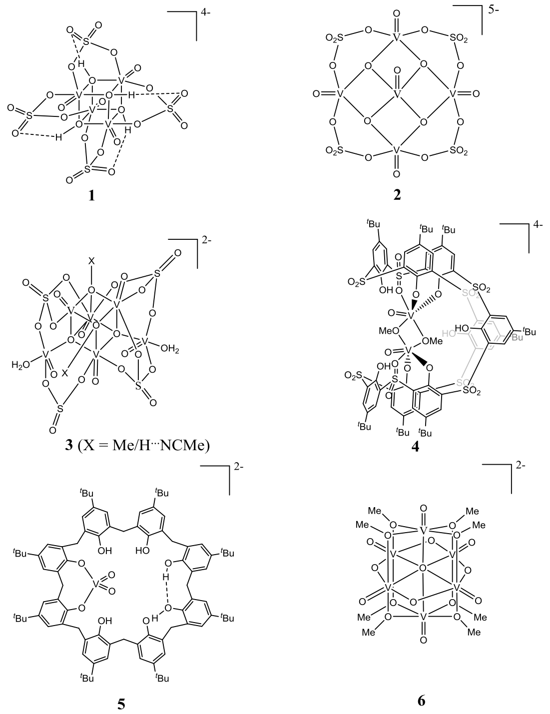

Chart 2 Products **1** - **6**.

Results and discussion

In the case of the reaction employing $[L^{4S}H_4]$:[V] = 1:4, crystals of $[NEt_4]_4[(VO)_4(\mu_3\text{-}OH)_4(SO_4)_4]\cdot{}^1/_2H_2O$ (**1**) suitable for X-ray diffraction were grown in *ca*. 70 % yield from a saturated solution of acetonitrile on prolonged standing at 0 °C. The molecular structure is shown in Figure 1, with selected bond lengths and angles given in the caption (for an alternative view see Figure S1, ESI).[13] Half of the formula above is unique and the molecule lies on a 2-fold axis. There is a central V_4O_4 distorted cubane core in which each of the V^{IV} centers adopts a distorted octahedral geometry with each coordinated by three μ_3-OH groups, one terminal oxygen and two oxygens from two of the four SO_4 tetrahedra that encompass the core. In the distorted cubane core, the O–V–O angles range from 75.33(19) to 75.89(16)°, V–O–V angles range from 102.39(18) to 102.95(17)° and V^{IV}–O terminal and bridging bond lengths of 1.580(4)/1.587(4) and 2.006(4) to 2.315(4) Å, respectively which are typical.[6-12] This sulfate-stabilized tetranuclear core carries a –4 charge, which is counter-balanced by four tetraethylammonium cations. The water molecule is very diffuse/partially occupied and lies on a special position, whereby it can make viable H-bonds with O(1), O(2) and their symmetry equivalents at 3.43 and 3.29 Å, respectively. There is also a noticeable 'leaning' of the sulfates towards the hydroxyl positions which is suggestive of further H-bonding. In the packing of **1**, a water molecule is encapsulated between four anions in the *b* direction, which results in a layer structure (see Figure S2, ESI). We note that vanadyl sulfates are rare, which is said to be due to problems associated with crystallization.[14] Recently, Mikuriya *et al* have reported the molecular structures of two anionic tetranuclear vanadyl sulfates,[15] whilst the cluster complex $[V_8O_{20}(4,4'\text{-}t\text{-Bubipy})]$ reported by Kodama and Ishii possesses a central core with a V_4 centre reminiscent of that in **1**.[16] A MOF containing a V_4 cubane-like core has also been reported.[17]

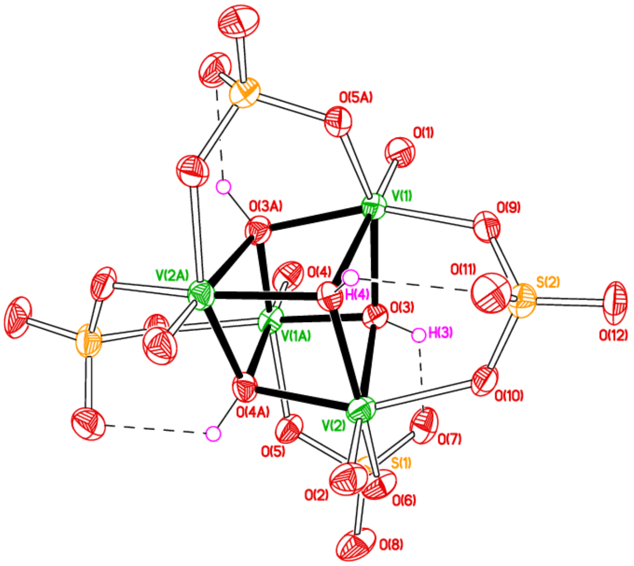

Figure 1. ORTEP diagram of the structure of **1**. Selected bond lengths (Å) and angles (°): V(1) – O(1) 1.580(4), V(1) – O(3) 2.016(4), V(1) – O(3A) 2.010(4), V(1) – O(4) 2.315(4), V(1) – O(5A) 2.006(4), V(1) – O(9) 2.009(4), V(2) – O(10) 2.011(4); O(1) – V(1) – O(3A) 102.7(2), O(1) – V(1) – O(4) 178.2(2), V(1) – O(3) – V(2) 102.64(17), V(1) – O(4) – V(2) 102.76(17), V(1) – O(9) – S(2) 131.2(2), V(2) – O(10) – S(2) 124.4(2). Symmetry code: A = –x, y, –z+½. $[NEt_4]^+$ cations and water molecule of crystallization omitted for clarity. Displacement ellipsoids are drawn at the 50% probability level.

Changing the $[L^{4S}H_4]$:[V] ratio to 1:6, led to the isolation of a mixed-valent $[V^{IV}{}_4V^V]$ umbrella-like cluster **2** similar to that reported by Xu *et al.*[15a] The Xu preparation involved solvothermal synthesis at 180 °C over a 5 day period, followed by subsequent cooling, whilst our procedure is complete within 12 h (refluxing methanol for 6 h, removal of volatiles and extraction into MeCN). Crystals of $[HNEt_3]_5[(VO)_5(\mu_3\text{-}O)_4(SO_4)_4]\cdot 4MeCN$ (**2**·4MeCN) were obtained from acetonitrile at 0 °C.[18,19] The vanadyl cap is the V^V centre, whilst each $[HNEt_3]^+$ cation binds to a sulfate oxygen, see Figure 2 (for an alternative view see Figure S3, ESI). The packing results in double layers of cations/anions in the *a*/*b* plane separated by layers of solvent of crystallization (see Figure S4, ESI).

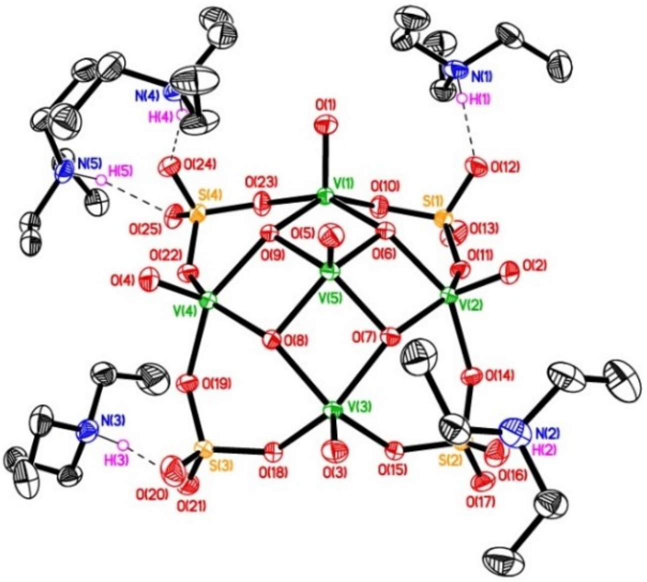

Figure 2. ORTEP diagram of the structure of **2**. Selected bond lengths (Å) and angles (°): V(1) – O(1) 1.593(3), V(1) – O(6) 1.962(2), V(1) – O(9) 1.960(2), V(1) – O(10) 1.983(3), V(1) – O(23) 2.007(3), V(5) – O(5) 1.597(2), V(5) – O(6) 1.865(2), V(5) – O(7) 1.877(2), V(5) – O(8) 1.885(2), V(5) – O(9) 1.870(2); O(1) – V(1) – O(6) 103.85(13), O(1) – V(1) – O(9) 105.70(12), O(10) – V(1) – O(23) 85.13(10), O(6) – V(5) – O(7) 83.49(10), O(8) – V(5) – O(9) 83.34(10). MeCN molecules of crystallisation and most H atoms omitted for clarity. Displacement ellipsoids are drawn at the 50% probability level.

When an excess of $VOSO_4$ was employed, typically $[L^{4S}H_4]$:[V] 1:30, the hexa-vanadate $[NEt_4]_2[(VO)_6(O)_2(SO_4)_4(OMe)(OH_2)]\cdot MeCN$ (**3**·MeCN) was reproducibly isolated on prolonged standing of a saturated MeCN solution at ambient temperature; use of $L^{6CH2}H_6$ also led to **3**.[20] The molecule **3** lies on a mirror plane (see figure 3) and either O(2) is methoxy and O(4) hydroxy (H-bonded to MeCN) or the reverse, *i.e.* the half occupancy for the methyl and MeCN (for an alternative view of **3** see Figure S5, ESI). The water molecules and vanadyl oxygens at O(9) and O(16) provide H-bonded links giving rise to wave-like 2D sheets of polyoxovanadate anions in the *b*/*c* plane (the cations fill the voids, see Figure S6, ESI).

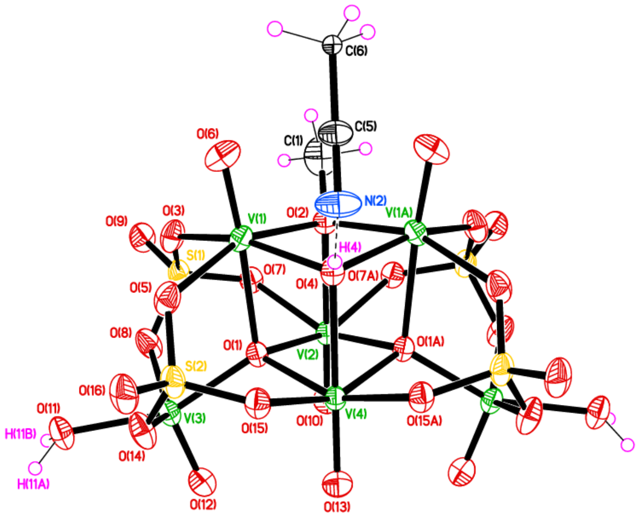

Figure 3. Molecular structure of **3**. Selected bond lengths (Å) and angles (°): V(1) – O(1) 2.283(3), V(1) – O(2) 2.004(3), V(1) – O(3) 2.041(3), V(1) – O(4) 2.001(2), V(1) – O(5) 2.044(3), V(1) – O(6) 1.595(3), V(2) – O(1) 1.999(3), V(2) – O(2) 2.364(4), V(2) – O(7) 2.047(3), V(2) – O(10) 1.583(4), O(1) – V(1) – O(2) 80.42(14), O(1) – V(1) – O(3) 80.40(12), O(1) – V(1) – O(4) 79.36(14), O(1) – V(1) – O(5) 79.75(12), O(1) – V(1) – O(6) 175.74(13), O(1) – V(2) – O(7) 89.02(11), O(1) – V(2) – O(10) 105.21(14), O(2) – V(2) – O(10) 174.78(19). Symmetry code A = x, –y+3/2, z. $[NEt_4]^+$ cations omitted for clarity. Displacement ellipsoids are drawn at the 50% probability level.

Use of sulfonylcalix[4]arene ($L^{4SO2}H_4$:V = 1:6) also led to complex **2**, but as the water solvate **2**$^{/}$ in good yield (*ca.* 70 %),[21] whilst subsequent extraction of the remaining residue into dichloromethane afforded upon crystallization at 0 °C the first example, albeit in low yield, of a metal complex of an SO_2-bridged calix[8]arene, namely $[HNEt_3]_2[H_2NEt_2]_2[VO(OMe)]_2$p-*tert*-butylcalix[8-$SO_2$]arene$H_2$] (**4**) – see Figure 4 for molecular structure (for an alternative view see Figure S7, ESI).[22] We note that thiacalix[8]arene ligands are known, but not their sulfonyl analogues.[23] The formation (and low yield) of **3** is due to the presence of a small amount of the parent $-SO_2$-bridged calix[8]arene in the calix[4]arene batch (see mass spectrum Figure S8, ESI). The molecule **4** lies on a center of symmetry, so half of the above formula is unique. The calix[8]arene makes four phenolate dative bonds to the two vanadyl centers (two to each); there are two non-coordinated phenol groups and two non-coordinated phenolates. The H(4) atom was readily found in the difference maps. The phenolic H(4) is involved in H-bonding to a neighbouring O on an SO_2 group, O(10). O(3) is a phenolate O, and accepts an H-bond from an $HNEt_3^+$ cation. An $H_2NEt_2^+$ cation also makes two pairs of bifurcated H-bonds with one connection to the O of an SO_2 group, the other to a phenolate O in each case. The clusters of V_2 anion and four cations are quite well separated from symmetry related units. Overall these stack in columns and layers built up by translation and inversion symmetry. The isolation of the SO_2-bridged calix[8]arene complex **4** is of key interest in terms of the potential accessibility of a new family of larger sulfonyl-bridged calix[8]arenes.

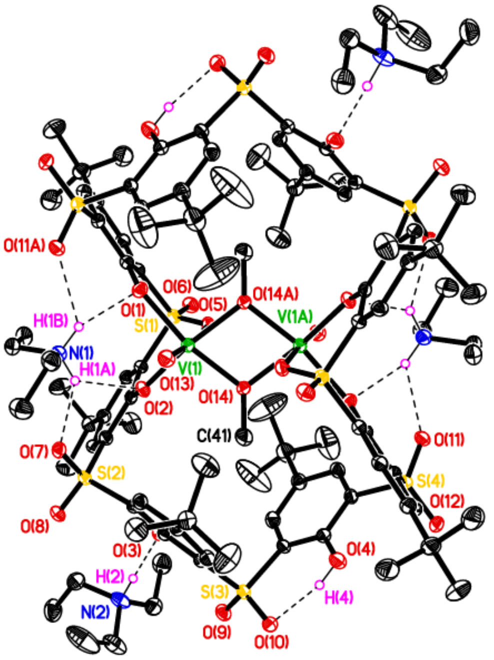

Figure 4. Molecular structure of **4**. Selected bond lengths (Å) and angles (°): V(1) – O(1) 2.041(2), V(1) – O(2) 2.020(2), V(1) – O(5) 2.287(2), V(1) – O(13) 1.608(2), V(1) – O(14) 1.960(2), V(1) – O(14A) 1.971(2), V(1)···V(1A) 3.0833(11); O(1) – V(1) – O(2) 89.15(9), V(1) – O(14) – V(1A) 103.30(9). Symmetry code A = –x+2, –y+2, –z+1. Displacement ellipsoids are drawn at the 40% probability level.

Increasing the size of the calix[*n*]arene to p-*tert*-butylcalix[8]arene $L^{8CH2}H_8$, in combination with $VOSO_4/Et_3N$, led to the formation of the yellow vanadium(V) complex $[HNEt_3]_2[V(O)_2L^8H_5]$ (**5**).[24] Single crystals suitable for an X-ray structure determination were grown from a saturated MeCN solution on prolonged standing (1 -2 days) at ambient temperature. The molecular structure is shown in Figure 5 (for an alternative view of **5** see figure S9, ESI). This complex was very robust and further reaction with $VOSO_4$/base resulted only in the isolation of **5**. Both cations H-bond to the vanadyl group, to each of the two vanadyl Os, whilst five calixarene phenol groups H-bond to their neighbours; O(6) is phenolate and accepts two H-bonds.

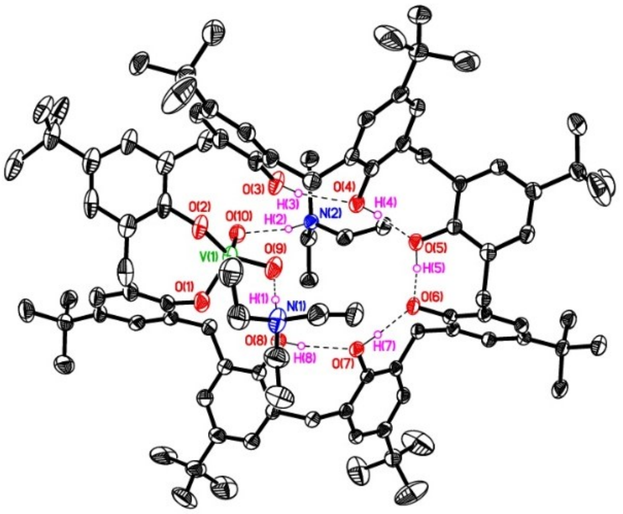

Figure 5. Molecular structure of **5**. Selected bond lengths (Å) and angles (°): V(1) – O(1) 1.817(3), V(1) – O(2) 1.801(3), V(1) – O(9) 1.628(3), V(1) – O(10) 1.632(3); O(1) – V(1) – O(2) 104.28(14). MeCNs of crystallization and most H atoms omitted for clarity. Displacement ellipsoids are drawn at the 50% probability level.

We then investigated the use of p-*tert*-butylhexahomotrioxacalix[3]areneH$_3$, $L^{CH2OCH2}H_3$, which following work-up (MeCN) afforded the known orange vanadyl complex $[VO(L^{CH2OCH2})]$ in good yield (*ca*. 70%).[25] We noted however that the mother-liquor was dark green, and on one occasion managed to grow dark green crystals from MeCN at 0 °C of the mixed-valent hexavanadate $[V^{IV}_2V^{V}_4O_{11}(OMe)_8]^{2-}$ (**6**), albeit in low yield (*ca*. 20 %), the molecular structure of which is shown in Figure 6.[26] The molecule sits on an inversion centre and is made up of a $[V_6O]$ core identical to that reported by Zubieta,[9c] but with the tris(hydroxymethyl)methane-derived chelating groups replaced by eight methoxides as in the calix[4]arene-supported Luneau structure. The complex $[V_6O_{10}(OH)(OMe)_8]$ has also been briefly mentioned.[27] The anion charge in **6** is balanced by two Et_3NH^+ cations generated from the base. There is also H-bonding between N–H···O between cations and anions. The presence of weak C–H···O interactions gives rise to an extended 3D network (see Figure S10, ESI).

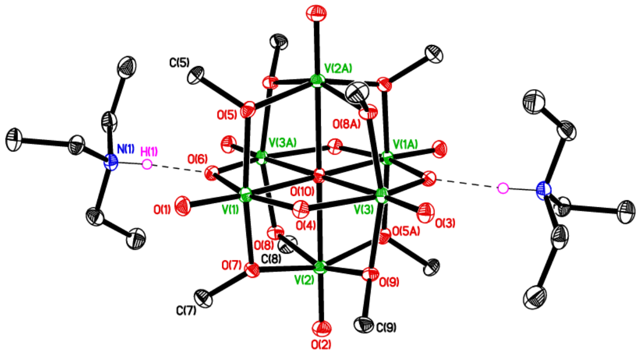

Figure 6. Molecular structure of **6**. Selected bond lengths (Å) and angles (°): V(1) – O(1) 1.6111(18), V(1) – O(4) 1.7054(18), V(1) – O(5) 1.9543(18), V(1) – O(6) 2.1002(18), V(1) – O(7) 1.9704(18), V(1) – O(10) 2.2455(4), V(2) – O(10) 2.3138(4); O(4) – V(1) – O(6) 156.34(8), O(1) – V(1) – O(10) 171.17(7), O(5) – V(1) – O(7) 159.67(8). Symmetry code A = –x+2, –y+1, –z+1. Most H atoms omitted for clarity. Displacement ellipsoids are drawn at the 50% probability level.

Electrochemistry

The DPV voltammogram of **2** in dry electrolyte (Figure 7 A) shows six oxidation peaks that can be assigned to isostructural vanadium species with varying V^{IV} content in compound **2** (Chart 2). This includes a fully reduced cluster species at the lowest potential (peak "a") and the oxidized cluster '$[VV_4]$' with vanadium (+5), generated during the scanning potential towards positive values. These redox peaks are attributed to successive one-electron oxidation processes. In the DPV backward scan (Figure S11 D) of **2** in the absence of H_2O, most of the redox transition are irreversible, indicating that compound **2** undergoes irreversible electrochemical oxidation upon applying high positive potential. This is further confirmed by the stability test carried out in dry electrolyte by applying 100 CV scans in the potential range where the compound **2** exhibits electrochemical activity. As demonstrated in Figure S12 A, the current associated with the redox transition of **2** (peaks "a-f") slightly decreases with increasing number of CV cycles. Yet, after recording the cyclic voltammogram, which was performed up to +2.0 V, no traces of deposited material was found on the surface of working electrode.

The compound **1** was subjected to the repetitive potential cycling in the same way as compound **2** (Figure S16). Not only did the colour of the vanadium solution change from dark violet (indicating the presence of $[V(H_2O)_6]^{2+}$) to pale yellow ($[VO(H_2O)_5]^{3+}$), but an insoluble film was formed at the electrode surface. Possibly, this is a vanadium oxide that can be generated electrochemically at the potential as low as 0.7 V *vs*. Ag/AgCl.[28] A significant difference is observed when the number of CV cycles increases for **1** and **2** in the absence of water. The anodic peak decreases and even disappears for **1**, while it slightly decreases for **2** (Figure S12 A). The compound **1** was observed to be much less stable upon polarization and in the presence of H_2O as compared to **2**. Also, DPV and CV scans of **1** in dry and water-containing electrolyte showed no activity for water oxidation (Figure S17).

The electrochemical water oxidation in the presence of the compound **2** was validated by the differential pulse, cyclic voltammetry and a bulk electrolysis. Since repetitive potential scanning of **2** in both dry electrolyte and in the presence of water (Figure S15) revealed a decrease in current recorded upon polarization, the electrode was cleaned in dry electrolyte after each CV, DPV and bulk electrolysis (BE) scan. Figure 7 A shows an increase in anodic current at about 1.4 V that can be assigned to water oxidation in the electrolyte:H_2O 10:1 v/v ratio. This anodic current does not increase with increasing concentration of **2** (Figure S11 B), indicating that **2** is not stable upon prolonged exposure to water (notice the electrode was cleaned in dry electrolyte after each DPV and CV scan to avoid accumulation of insoluble products of electrochemical degradation of **2** that passivate the glassy carbon electrode). New signals were acquired in voltammograms of **2** in the presence of water (Figure 7), which are *(1)* the shift of the potential onset for a-f peaks (labelled in Figure 7 A as a'-f'); *(2)* and the broadening of right shoulder of b' being the shifted c and d peaks. A new oxidation peak at ~ -0.4 V represents anodic activity of the product formed between compound **2** and H_2O, however its identification requires further analysis using complementary spectroscopic techniques (the signal is very weak and cannot be detected by conventional cyclic voltammetry, Figure 7 B).

The four-electron oxidation of H_2O requires the accumulation of multiple redox equivalents at the catalytic entity. This could be regulated by the simultaneous transfer of electrons and protons, enabling proton-coupled electron transfer (PCET). Such a process was identified in the Ru picoline complex $[Ru(HL)(pic)_3]^+$,[29] and resulted in significantly decreased redox potentials of the metal complex, and hence lowered the catalytic onset potential at which H_2O is being oxidized. Assuming that a similar reaction pathway takes place during water discharge in the presence of compound **2**, in order to generate the catalytically active intermediate, $[HNEt_3]_5[(VO)_5(\mu_3\text{-}O)_4(SO_4)_4]\cdot 4CH_3CN$ (**2**·4MeCN) has to undergo the ligand−H_2O exchange, analogous to the process observed for $[Ru(HL)(pic)_3]^+$. Other than ligand exchange, this positive shift of the V^{4+}/V^{5+} redox peaks (a', b' and c' in Figure 7 A) could be related to the PCET with a proton generated simultaneously during water oxidation. Both hypotheses however need further analysis supported by spectroscopy in order to be fully verified.

The amount of produced O_2 was measured only for the comparison purpose using a real-time electrochemical quartz crystal microbalance (EQCM), recorded simultaneously during CV scans and after the bulk electrolysis. Other electrochemical methods and mathematical models usually applied for an estimation of an evolved O_2 cannot be used due to the instability of the catalysts under potential. Also, the water oxidation reaction in the presence of **2** does not meet the requirements of pseudo-first order kinetics, such as it does not show direct proportionality of WO peak current with the increasing concentration of **2**; both the catalyst peak current and water discharge current depend the potential scan rate in whole range of scanning.[30] In the presence of H_2O for compound **2**, O_2 evolution could immediately be detected (Figure 8 B). The low O_2 evolution yields were due to the decomposition of $[HNEt_3]_5[(VO)_5(\mu_3\text{-}O)_4(SO_4)_4]\cdot 4CH_3CN$ (**2**·4MeCN) resulting in unproductive reaction pathways. After subtraction of background EQCM scans (performed in the same conditions in absence of water), O_2 was quantified using the Sauerbrey equation applied to EQCM data (Figure 8 A) and presented in Table 1:

$$\Delta f = \frac{-2f_0^2}{A\sqrt{\rho\mu}}\Delta m \quad (1)$$

Where f_0 is resonant frequency of crystal's fundamental mode (the carbon-coated resonator used in this analysis has f_0 = 7.995 MHz fundamental frequency (provided by manufacturer), A is a crystal surface area (= 0.1963 cm^2), ρ is crystal density (= 2.684 g/cm^3), μ is shear modulus of quartz (= 2.947 × 10^{11} g/cm × s^2), Δf is observed frequency change (Hz) and Δm is change in electrode mass per unit area (g/cm^2).

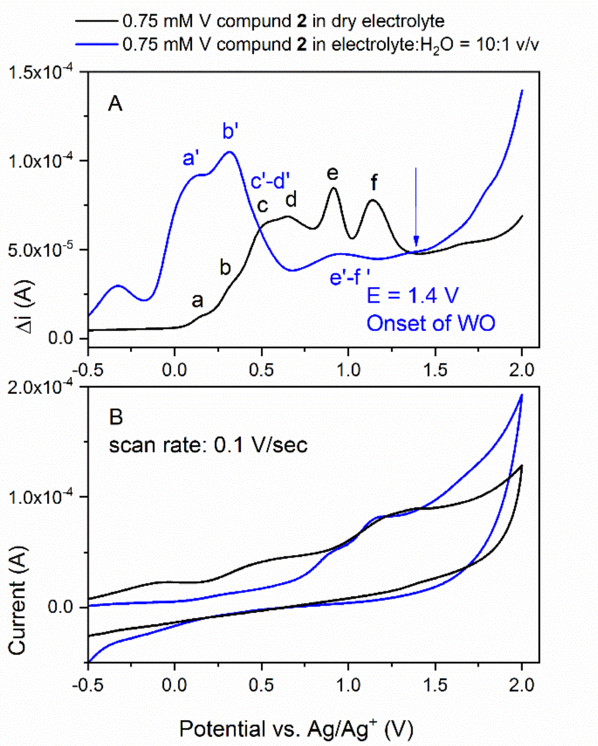

Figure 7. DPV scan (A) and CV (B) of **2**: 0.75 mM in 0.1M $TEABF_4$/ dry CH_3CN, *vs* Ag/Ag^+ (0.681 *vs* SHE) in the absence (black) and presence of water (blue) at the electrolyte:water = 10:1 v/v; potential scan rate 0.1 V/s.

Although, the initial rate of O_2 evolution was shown to be proportional to the concentration of **2** (Figure 8 A and B), the requirements to obtain TOF values from mathematical models applied to the cyclic voltammetry tests are not fulfilled.[30] It is assumed that the concentration of compound **2** changes on increasing scan rate due to slow progressing decomposition both in the absence (Figure S13 A) and the presence of water (Figure S13 B). The O_2 rate constant was approximated from the bulk electrolysis tests using the linear slope of *charge* = f(*time*) plot (Figure S14). The slope is expressed in Coulomb per second ($C\ s^{-1}$) and was calculated for different concentrations of **2** (Table 1). Furthermore, O_2 evolution rate (*k*O2; mmol s^{-1}) was quantified by applying the Faraday's law of electrolysis ($n = Q/F \times z$; where Q is charge in Coulombs, F is Faraday constant C mol^{-1}, z is a number of the electron exchanged = 4 in this case). Finally, the TOF was calculated according to correlation: TOF [s^{-1}] = (rate of O_2 evolution mmol s^{-1})/mmol of cat. [29] and presented in Table 1. The measured rate constant (kO_2) at various concentrations of **2** subsequently converted to the turnover frequency (TOF) are within the range of 22-3.2 × 10^{-5} s^{-1}. The TOFs obtained for **2** are significantly lower than reported for various homogeneous water oxidation catalysts, such as Ru complexes (1.16 s^{-1}) [29] or [Ru(pdc)(pic)$_3$] with 0.23 s^{-1}.[31] Consequently, the turnover numbers (TONs) calculated from the Sauerbrey equation applied to EQCM data (and defined as the mol of produced O_2 per mol of catalyst) are very low (Table 1), as compared to the referred Ru complexes.

At this stage, any conclusions related to the catalytic activity of compound **2** for the electrochemical water oxidation would be premature. One can conclude that several successive one-electron oxidation processes involving different metal centers precede the catalytic wave, could suggest that the catalytic pathway involves multiple sites, but it does not exclude a single-site process.

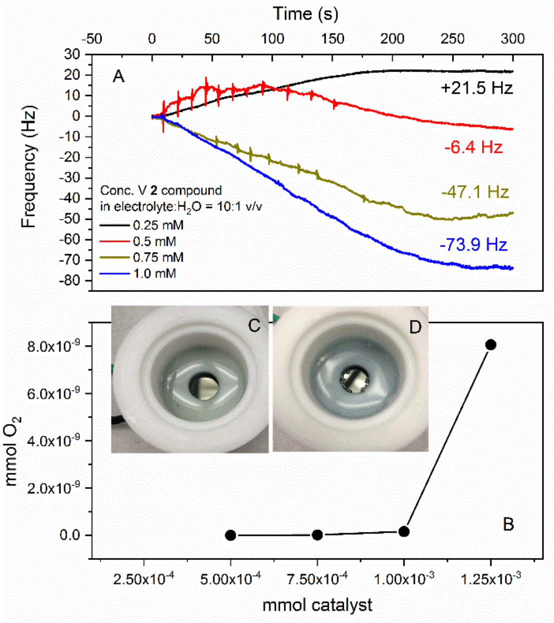

Figure 8. QCM scan (A) at 0.25, 0.5, 0.75 and 1mM of **2**: 0.75 in 0.1M TEABF$_4$ /MeCN: water = 10:1 v/v; recorded after bulk electrolysis carried out at 1.4 V (0.681 V *vs.* SHE) for 15 min; mmol of produced O_2 calculated based on adsorption of O_2 monolayer on QCM

steps.

resonator calculated using Sauerbrey equation (1) as a function of mmol of **2** (B); the photos show QCM electrochemical cell after bulk electrolysis in the absence (C) and the presence of water (D).

Figure 9 demonstrates the electrochemical activity of compound **3** in the absence (black) and the presence of water (blue). The electrochemical behaviour of **3** in dry electrolyte solution is very similar to that of **2** (Figure 7). Similar to the compound **2**, the current in the potential range of the overlapped oxidation waves of V^{+4}/V^{+5} species decrease with a progression of the CV scan numbers.

A completely different activity of this compound is observed when 10 % v/v of water is introduced at the same concentration of electrolyte. A significantly larger current related to the V^{+4}/V^{+5} transitions than those measured in dry electrolyte suggests a greater number of electrons exchanged, at least on the short CV timescale. Also, the oxidation potential of V^{4+} species is shifted to more negative values and a significantly different degree of electrochemical reversibility (reduction peaks of V^{5+} at various sites appear within 1.1 and 0.5 V) in the presence of water. If it is assumed that the diffusion coefficient of compound **3** in both electrolytes are similar, the increase in current is likely due to the increase of electrons transferred. Opposite to the test done in the presence of water (Figure 9, blue scan), the reduction current related to the formation of V^{4+} in reverse CV scan is not observed in the absence of water. This could indicate that protons introduced during WO process participate in charge balance (the WO process is not clearly identified in CV of **3** as it overlaps with anodic current related to several V^{4+} centers). More importantly, the magnitude of current increases with increasing number of CV scans, which is quite remarkable considering that other compounds tested in this work showed instability in both dry and wet electrolyte. The systematic increase of measured current can be related to the increasing number of generated protons during water discharge. These protons are believed to participate in redox activity of vanadyl, similar to processes observed for $VOSO_4$ in aqueous KCl solution:[32]

$$H_3V_2O_7^- + 3H^+ + 2e^- \leftrightarrow V_2O_4 + 3H_2O \qquad (2)$$

The negative shift of the onset potential of vanadyl oxidation (Figure 9, blue) with decreasing pH has been reported by the same group.[32] The linear fit of the Pourbaix diagram (where the onset potential for vanadyl oxidation was plotted *versus* pH) revealed that this process involves three protons and two electrons and is consistent with proposed reaction (Equation 2).

Overall, examining these curves one can appreciate that the current increase is attributed to the change of electrochemical overlapped

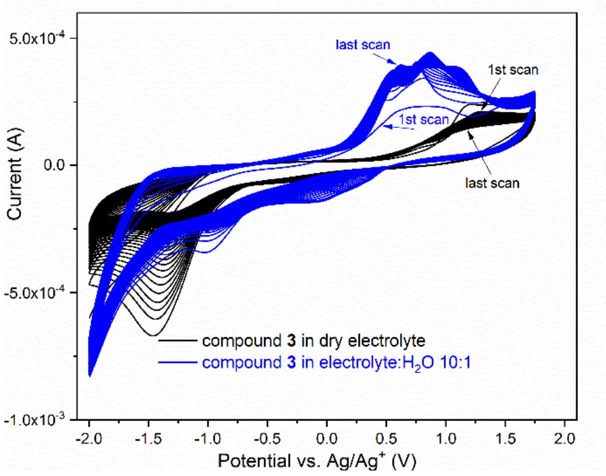

Figure 9. CV of compound **3** in dry electrolyte (black) and the presence of water (blue) recorded at the scan rate of 0.1 V/s.

Table 1. Quantification of O_2 monolayer produced after bulk electrolysis in the presence of compound **2** calculated form EQCM scans; the rate of O_2 evolution was quantified based on BE and the mole of produced O_2 was calculated from Faraday law of electrolysis; turnover number (TON) and turnover frequency (TOF) are quantified based on EQCM and BE, respectively.

Compound 2 concentration (mM)	Catalyst mmol	mmol O_2 based on EQCM [a]	TON (mmol O_2/ mmol cat.) from QCM	Rate of O_2 evolution C s^{-1} [b]	Rate of O_2 evolution mmol O_2 s^{-1} [c] from BE	Turnover frequency TOF s^{-1} [d]
0.25	5.0×10^{-4}	0	0	6.3×10^{-6}	1.6×10^{-8}	3.2×10^{-5}
0.5	7.5×10^{-4}	2.2×10^{-11}	2.9×10^{-8}	6.4×10^{-6}	1.6×10^{-8}	2.1×10^{-5}
0.75	1.0×10^{-3}	1.6×10^{-10}	1.5×10^{-7}	8.2×10^{-6}	2.1×10^{-8}	2.1×10^{-5}
1	1.2×10^{-3}	8.1×10^{-9}	6.4×10^{-6}	1.1×10^{-5}	2.8×10^{-7}	2.2×10^{-4}

[a] based on monolayer of O_2 generated on EQCM resonator after bulk electrolysis (BE) carried out at the 1.41 V for 15 min; after subtraction of blank (BE carried out in dry electrolyte at the same conditions).
[b] based on the slope of *charge* = f(*time*) acquired from bulk electrolysis; Fig. S14 in supporting information; due to electrochemical instability of compound the blank BE curve was recorder for 2 compound in dry electrolyte and subtracted from the test carried out in electrolyte:H_2O = 10:1 v/v.
[c] mmol of O_2 calculated from Faraday's law of electrolysis: $n = Q/F \times z$ (where Q – is charge in Coulombs, F is Faraday constant C/mol, z is a number of electrons exchanged ($z = 4$ in this case)
[d] TOF was calculated according to the formula: [29] TOF [s^{-1}] = (rate of O_2 evolution mmol s^{-1})/mmol of cat.

Magnetism

Dc magnetic susceptibility measurements were performed on powdered microcrystalline samples of **1**-**3** in the T = 300 - 2 K temperature range, in an applied field (B) of 0.5 T (for **1** - **2**) and 0.1 T for **3**, and are plotted as their $\chi_M T$ products *versus* T in Figure 9, where $\chi_M = M/B$, and M is the magnetisation of the sample. Samples were stored and loaded into gelatine capsules in a glove box to prevent oxidation.

For **1** and **2**, the room temperature $\chi_M T$ value of 1.44 cm^3 mol^{-1} K is in a good agreement with the sum of Curie constants expected for four non-interacting V(VI) centres, assuming g = 1.98 (1.47 cm^3 mol^{-1} K). Upon cooling, the $\chi_M T$ values of both remain relatively constant until T ~125 K, wherefrom they decrease to values of 0.03 and 0.7 cm^3 mol^{-1} K at 2 K for **1** and **2**, respectively. This behaviour is consistent with antiferromagnetic exchange interactions between the metal centres, and the presence of diamagnetic ground states, in both cases. Fits of the experimental susceptibility data to spin-Hamiltonian (1) [where the indices i and j refer to the V(IV)) ions, μ_B is the Bohr magneton, B is the applied magnetic field, g is the g-factor of the V(IV) ions (2.00), $\hat{S}$ is a spin operator and J is the isotropic exchange interaction parameter] using the coupling schemes outlined in Figure 10 afford the best fit parameters J_1 = –3.73 cm^3 mol^{-1} K and J_2 = –7.43 cm^3 mol^{-1} K for **1**, and J_1 = –1.6 cm^3 mol^{-1} K for **2**, with g fixed at g = 1.98. We note with interest that the data for complex **2** are different to that reported recently by Xu and co-workers for the analogous species $[V^VV^{IV}_4O_5(\mu_3\text{-}O)_4(SO_4)_4(en)]^{5-}$ (en = ethylenediamine).[15a] In the latter paper, the authors suggest the presence of both ferro- and antiferromagnetic exchange and a non-zero spin ground state, but this is not possible in a square with four-fold symmetry. We also note that complex **2** is both air- and moisture-sensitive and handling out-with a glovebox leads to sample degradation.

$$\hat{H} = \mu_B B \sum_i g_i \hat{S}_i - 2 \sum_{i.j<i} J_{ij} \hat{S}_i \hat{S}_j \qquad (1)$$

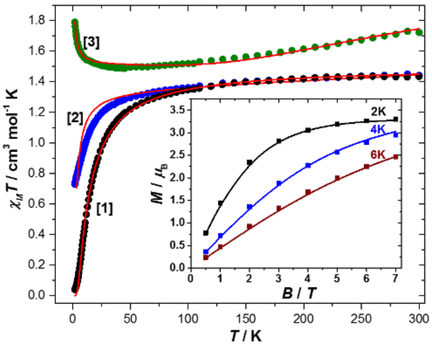

Figure 9. Plot of $\chi_M T$ versus T for complexes **1**-**3** measured in the T = 300 - 2 K temperature range in an applied field of 0.5 T (for **1** - **2**) and 0.1 T for **3**. (Inset) Plot of the VTVB data for **3** in the T = 2 – 6 K and B = 0 – 7 T, temperature and field ranges The solid red lines represent best fits of the experimental data to spin-Hamiltonian (1). See text for details.

The experimental data for **3** are rather different. The room temperature $\chi_M T$ value of 1.72 cm^3 mol^{-1} K at 300 K is below that expected for six non interacting V(IV) centres (2.21 cm^3 mol^{-1} K for g = 1.98), and upon lowering temperature the value first decreases to 1.48 cm^3 mol^{-1} K at 45 K, then increases to 1.79 cm^3 mol^{-1} K at 2 K. This is characteristic of competing ferromagnetic and antiferromagnetic exchange interactions. To better define the low-temperature magnetic properties of **3**, low temperature variable-temperature-and-variable-field (VTVB) magnetization data were measured in the T = 2 - 6 K and B = 0 - 7 T temperature and field ranges (Figure 10, inset). At the highest investigated field (7 T) and the lowest investigated temperature (2 K), the magnetization of **3** is 3.3 μ_B. A simultaneous fit of the susceptibility and magnetization data employing spin-Hamiltonian (1) and the model shown in Figure 10 (with g fixed at g = 1.98) afforded the best-fit parameters J_1 = –29 cm^{-1}, J_2 = –187.6 cm^{-1}, J_3 = +0.43 cm^{-1} and J_4 = +0.17 cm^{-1}. These values are in agreement with those derived for a structurally analogous hexametallic V(IV) compound reported by Miras *et al.*[33]

The experimentally derived coupling constants for **1**-**3** are in also agreement with magneto-structural correlations previously developed for hydroxo-bridged dinuclear oxovanadium(IV) species by Plass and Rodriguez-Fortea.[34] These studies showed that for $[V(IV)_2O_2]$ species, with a magnetic d_{xy} orbital, both direct and superexchange mechanisms are operative, the former being strongly antiferromagnetic and the latter weakly ferro- or antiferromagnetic.

The nature and magnitude of exchange being dependent upon geometry; more specifically on (i) the orientation of the vanadyl groups (V=O) with respect to the bridging V_2O_2 plane, and (ii) the relative orientation of the vanadyl groups (V=O) with respect to each other.

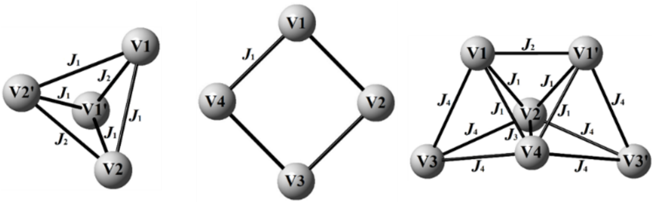

Figure 10. Scheme defining the different exchange coupling constants used to fit the experimental data of compounds **1** – **3** (left to right, respectively). The different *J* values are defined according to the magneto-structural correlation developed by Plass and Rodriguez-Fortea. See reference 38 for full details.

Experimental

All manipulations were performed under N_2 using standard Schlenk techniques and dried, deoxygenated solvents. The ligands $\mathbf{L}^{\mathbf{6CH2}}H_6$, $\mathbf{L}^{\mathbf{8CH2}}H_8$, $\mathbf{L}^{\mathbf{CH2OCH2}}H_3$ and $\mathbf{L}^{\mathbf{4SO2}}H_4$ were prepared as reported in the literature,[35] whilst the ligand $\mathbf{L}^{\mathbf{4S}}H_4$ was obtained from TCI UK.

For **1**, a typical synthesis involved thiacalix[4]arene (0.15 mmol), $VOSO_4$ (0.60 mmol) and Et_4NOH (1M in H_2O, 10.8 mmol) which were refluxed together in methanol (30 mL) under a nitrogen atmosphere. The base employed can be either Et_3N or Et_4NOH. Removal of solvent followed by work-up (extraction) in acetonitrile (30 mL) afforded blue crystalline **1** in *ca.* 70 % yield. Found C 30.39, H 7.02, N 4.35, S 9.96; $C_{32}H_{85}N_4O_{24.5}S_4V_4$ requires C 30.74, H 6.85, N 4.48, S 10.26%. IR *v*(V=O) 981s cm^{-1}. M.S. (ASAP, solid): 721 (Anion).

For **2**, as for **1** but using thiacalix[4]arene (0.15 mmol), $VOSO_4$ (0.90 mmol) and Et_3N (10.8 mmol). Yield *ca.* 85 %; Found C 31.09, H 6.27, N 8.55; $C_{38}H_{92}N_9O_{25}S_4V_5$ **2**·4MeCN: requires C 31.30, H 6.36, N 8.65%. IR *v*(V=O) 1019s cm^{-1}. M.S. 671 (Anion – SO_4 – O).

For **3**, as for **1** but using thiacalix[4]arene (0.15 mmol), $VOSO_4$ (4.50 mmol) and Et_4NOH (1M in H_2O, 10.8 mmol). Yield *ca.* 60 %; Found C 19.65, H 2.75, N 3.64; $C_{19}H_{31}N_3O_{28}S_4V_6$ requires C 19.28, H 2.64, N 3.55%. IR *v*(V=O) 1024s cm^{-1}. M.S. 737 (Anion – SO_4 – V).

For **4**, as for **1** but using sulfonylcalix[4]arene (0.15 mmol), $VOSO_4$ (0.90 mmol) and Et_3N (10.8 mmol). Extraction in to acetonitrile (30 mL) afforded **2'**·H_2O Found C 27.52, H 6.45, N 5.34; **2'**·H_2O: $C_{30}H_{82}N_5O_{26}S_4V_5\cdot H_2O$ requires C 27.46, H 6.40, N 5.19%. A second extraction of the residue with CH_2Cl_2 (30 mL) afforded **4**. Yield *ca.* 8 %; Found C 54.57, H 6.94, N 2.57; $C_{102}H_{152}N_4O_{28}S_8V_2$ requires C 54.67, H 6.84, N 2.50%. IR *v*(V=O) 1019s cm^{-1}. M.S. (+ve CI): 1794 (M^+ - $2Et_2NH_2$ – $2Et_3NH$ – 2OMe – 2O).

For **5**, as for **1** but using p-*tert*-butylcalix[8]areneH$_8$ (0.15 mmol), $VOSO_4$ (0.60 mmol) and Et_3N (10.8 mmol). Yield *ca.* 75 %; Found C 75.23, H 9.09, N 2.92; $C_{104}H_{147}N_4O_{10}V$ (sample dried *in vacuo* for 2 h - 2MeCN) requires C 75.05, H 8.90, N 3.36%. IR *v*(V=O) 1019s cm^{-1}. M.S. (nano-ESI, -ve): 1362 (Anion – O), 1295 (Anion – V – 2O). ^1H NMR (CD_3CN) δ: 7.30 (d, J_{HH} 2.4Hz, 1H, aryl*H*), 7.23 (m, 2H, aryl*H*), 7.21 (m, 2H, aryl*H*), 7.17 (d, J_{HH} 2.4Hz, 1H, aryl*H*), 7.14 (d, J_{HH} 2.4Hz, 2H, aryl*H*), 7.11 (s, 2H, aryl*H*), 7.05 (bs, 11H, aryl*H* + O*H*), 6.96 (d, J_{HH} 2.4Hz, 1H, aryl*H*), 6.91 (d, J_{HH} 2.8Hz, 1H, aryl*H*), 5.78 (d, $^2J_{HH}$ 13.0 Hz, 2H, *endo*-CH_2), 5.44 (d, $^2J_{HH}$ 11.4 Hz, 2H, *endo*-CH_2), 5.35 (d, $^2J_{HH}$ 14.0 Hz, 2H, *endo*-CH_2), 4.47 (d, $^2J_{HH}$ 12.0 Hz, 2H, *endo*-CH_2), 3.84 (bs, 2H, N*H*), 3.42 (d, $^2J_{HH}$ 13.0 Hz, 2H, *exo*-CH_2), 3.35 (d, $^2J_{HH}$ 11.4 Hz, 2H, *exo*-CH_2), 3.33 (d, $^2J_{HH}$ 14.0 Hz, 2H, *exo*-CH_2), 3.20 (d, $^2J_{HH}$ 12.0 Hz, 2H, *exo*-CH_2), 2.94 (q, J_{HH} 6.8 Hz, 12H, NCH_2), 1.21 – 1.13 (overlapping signals, 90H, NCH_2CH_3 + $C(CH_3)_3$).

For **6**, as for **1** but using p-*tert*-butylhexahomotrioxacalix[3]areneH$_3$ (0.15 mmol), $VOSO_4$ (0.9 mmol) and Et_3N (10.8 mmol). Extraction into acetonitrile (30 mL) afforded [VO($L^{CH2OCH2}$)] (70 %) and **6** (*ca.* 20 %). The products were separated by fractional crystallization. Found C 26.82, H 5.31, N 4.18; $C_{20}H_{56}N_2O_{19}V_6$ (sample recrystallized from acetonitrile as ·MeCN solvate) requires C 27.08, H 6.09, N 4.30%. IR *v*(V=O) 963s cm^{-1}. M.S. (+ve, CI): 668 (Anion – 2OMe), 637 (Anion – 3OMe), 606 (Anion – 4OMe), 575 (Anion – 5OMe), 544 (Anion – 6OMe).

Conclusions

In summary, we have synthesized a range of vanadyl-containing species with some fascinating structures, and observed that subtle changes in the reaction stoichiometry when using a particular calixarene template can lead to the isolation of quite different products. Such species possess intriguing magnetism and electrochemistry, whilst preliminary screening for water oxidation reveals that **2** containing a distorted V_4O_4 type core exhibits some activity however its TOF and TON were still significantly below that of currently competing homogenous and heterogeneous WO catalysts. The overpotential for the electrochemical oxidation of water in the presence of compound **2** was not lower when compared to reported literature. All compounds except **3** showed more or less progressing instability in dry electrolyte that was attributed to the irreversible oxidation of vanadium moiety, resulting in some cases in the formation of solid deposits of vanadium oxide on the electrode. The compound **3** exhibited significantly higher electrochemical activity and stability of vanadium centers in the presence of water. This is speculated to be due to the increased number and the rate of electrons exchanged, facilitated by protons generated in the WO process.

In addition here, we report the isolation of the first example of a metal complex of a sulfonyl-bridged calixarene, which has potential to open up a new field of exploration in calix[8-SO_2]arene coordination chemistry.

Conflicts of interest

There are no conflicts to declare.

Acknowledgements

The Advanced Light Source is supported by the Director, Office of Science, Office of Basic Energy Sciences, of the U.S. Department of Energy under Contract No. DE-AC02-05CH11231. Dr Simon Teat is thanked for technical help at the ALS. The EPSRC National Crystallographic Service at Southampton and the EPSRC National Mass Spectrometry Service at Swansea are thanked for data collection. The EPSRC is thanked for an Overseas Travel Grant (to CR).

Notes and references

‡ Footnotes relating to the main text should appear here. These might include comments relevant to but not central to the matter under discussion, limited experimental and spectral data, and

crystallographic data. CCDC 1574239-1574245 contain the supplementary crystallographic data for this paper.

1 J. M. Winter and B. S. Moore, *J. Bio. Chem*. 2009, **284**, 18577-18581.

2 See for example, (a) G. J. Colpas, B. J. Hamstra, J. W. Kampf and V. L. Pecorara, *J. Am. Chem. Soc*. 1996, **118**, 3469-3478. (b) V. Conte, O. Bortolini, M. Carraro and S. Moro, *J. Inorg. Biochem*. 2000, **80**, 41-49.

3 See C. Redshaw. *Dalton Trans*. 2010, **39**, 5595-5604 and references therein.

4 (a) D. H. Homden and C. Redshaw, *Chem. Rev*. 2008, **108**, 5086-5130. (b) Coordination Chemistry and Applications of Phenolic Calixarene–metal Complexes. Y. Li, K.-Q. Zhao, C. Redshaw, B. A. Martínez Ortega, A. Y. Nuñez, T. A. Hanna in Patai's Chemistry of Functional Groups. Wiley 2014.

5 Aronica, G. Chastanet, E. Zueva, S. A. Borshch, J. M. Clemente-Juan, D. Luneau, *J. Am. Chem. Soc*. 2008, **130**, 2365-2371.

6 See for example, (a) B. Castellano, E. Solari and C. Floriani, *Organometallics* 1998, **17**, 2328-2336. (b) C. Limberg, *Eur. J. Inorg. Chem*. 2007, 3303-3314 and references therein. (c) N. de Silva, S. –J. Hwang, K. A. Durkin and A. Katz, *Chem. Mater*. 2009, **21**, 1852-1860. (d) C. Redshaw, M. R. J. Elsegood, J. A. Wright, H. Baillie-Johnson, T. Yamato, S. De Giovanni and A. Mueller, *Chem. Commun*. 2012, **48**, 1129-1131. (e) C. Redshaw, M. J. Walton, D. S. Lee, C. Jiang, and M. R. J. Elsegood and K. Michiue, *Chem. Eur. J*. 2015, **21**, 5199-5210.

7 M. –P. Santoni, G. La Ganga, V. M. Nardo, M. Natali, F. Puntoriero, F. Scandola, S. Campagna, *J. Am. Chem. Soc*. 2014, **136**, 8189-8192.

8 (a) V. W. Day, W. G. Klemperer, D. J. Maltbie, *J. Am. Chem. Soc*. 1987, **109**, 2991-3003. (b) V. W. Day, W. G. Klemperer, O. M. Yaghi, *J. Am. Chem. Soc*. 1989, **111**, 4518-4519. (c) V. W. Day, W. G. Klemperer, O. M. Yaghi, *J. Am. Chem. Soc*. 1989, **111,** 5959-5961. (d) Y. Hayashi, *Coord. Chem. Rev*. 2011, **255**, 2270-2280 and references therein.

9 (a) M. I. Khan, Q. Chen, J. Zubieta, *Inorg. Chem*. 1992, **31**, 1556-1558. (b) M. I. Khan, Q. Chen, D. P. Goshorn, H. Höpe, S. Parkin, J. Zubieta, *J. Am. Chem. Soc*. 1992, **114**, 3341-3346. (c) Q. Chen, D. P. Goshorn, C. P. Scholes, X. –L. Tan, J. Zubieta, *J. Am. Chem. Soc*. 1992, **114**, 4667-4681. (d) M. I. Khan, Q. Chen, D. P. Goshorn, J. Zubieta, *Inorg. Chem.* 1993, **32**, 672-680. (e) M. I. Khan, Q. Chen, D. P. Goshorn, H. Hope, S. Parkin, C. J. O'Conner, J. Zubieta, *Inorg. Chem.* 1993, **32**, 2929-2937. (f) M. I. Khan, J. Zubieta, *Prog. Inorg. Chem*. 1995, **43**, 1-149.

10 (a) D. Hou, K. S. Hagen, C. L. Hill, *J. Am. Chem. Soc*. 1992, **114**, 5864-5866. (b) D. Hou, K. S. Hagen, C. L. Hill, *J. Chem. Soc., Chem. Commun*. 1993, 426-428.

11 M. Mikuriya, T. Kotera, F. Adachi, S. Bandow, *Chem. Lett*. 1993, 945-948.

12 L. J. Batchelor, R. Shaw, S. J. Markey, M. Helliwell, E. J. L. McInnes, *Chem. Eur. J*. 2010, **16**, 5554-5557.

13 For **1**$\cdot{}^1/_2H_2O$: $C_{32}H_{85}N_4O_{24.5}S_4V_4$, M = 1250.03, monoclinic, $C2/c$, a = 21.424(6), b = 11.429(3), c = 21.431(6) Å, β = 90.541(5)°, V = 5247(2) Å^3, Z = 4, μ(Mo-Kα) = 0.93 mm^{-1}, 23195 reflections measured, λ = 0.71073 Å, 5418 unique, R_{int} = 0.154, $R_1[I>2\sigma(I)]$ = 0.071, wR_2 (all data) = 0.200.

14 D. Pitzschke, J. Wang, R. –D. Hoffmann, R. Pöttgen, W. Bensch, *Angew. Chem. Int. Ed*. 2006**,** **45**, 1305-1308.

15 (a) S. Zhou, H. Wan, G. Hu, Y. Zhang, Y. Liu, H. Miao, D. Zhu, Y. Xu, *Dalton Trans*. 2015, **44**, 8605-8608 and references therein. (b) M. Mikuriya, M. Fukutani, D. Yoshioka, *X-ray Structure Analysis Online* 2015, **31**, 33-36. (c) M. Mikuriya, M. Fukutani, M. Omote, D. Yoshioka, R. Mitsuhashi, *X-ray Structure Analysis Online* 2016, **32**, 15-17.

16 (a) S. Kodama, N. Taya, Y. Inoue, Y. Ishii, *Inorg. Chem.*2014, **53**, 2754-2756. (b) S. Kodama, N. Taya, Y. Inoue, Y. Ishii, *Inorg. Chem*. 2016, **55**, 6712-6718.

17 A MOF containing a V_4O_8 cubane core has been reported for which the bond lengths are V – O$_{terminal}$ 1.593(3) Å, V – O$_{bridging}$ 1.865(3) Å, and V – O – V/ O – V – O angles in the range 78 – 102 °, see C. Dey, R. Das, P. Poddar, R. Banerjee, R. *Cryst. Growth Des*. 2012, **12**, 12-17.

18 For **2**·4MeCN: $C_{38}H_{92}N_9O_{25}S_4V_5$, M = 1458.14, orthorhombic, $P2_12_12_1$, a = 13.4462(15), b = 13.5404(16), c = 35.104(4) Å, V = 6391.3(13) Å^3, Z = 4, μ(Mo-Kα) = 0.91 mm^{-1}, λ = 0.71073 Å, 69277 reflections measured, 17270 unique, R_{int} = 0.041, $R_1[I>2\sigma(I)]$ = 0.035, wR_2 (all data) = 0.083. Racemic twin with major component 79.3(11)%.

19 For **2**·2.75H_2O, a provisional data set due to poor crystal quality: $C_{32}H_{80}N_4O_{25}S_4V_5\cdot 2.75H_2O$, M = 1352.05, tetragonal, $P4/ncc$, a = b = 13.7685(16), c = 39.530(7) Å, V = 7494(2) Å^3, Z = 4, μ(Mo-Kα) = 0.773 mm^{-1}, λ = 0.71073 Å, 13138 reflections measured, 1209 unique, R_{int} = 0.37. The vanadium umbrella complex connectivity is established as **2** and also the presence of the $[NEt_4]^+$ cations and some water of crystallization, but the relative stoichiometry of the individual components is not confidently established.

20 For **3**: $C_{19}H_{51}N_3O_{27}S_4V_6$, M = 1183.35, monoclinic, $P2_1/m$, a = 11.3206(8), b = 19.3232(13), c = 11.4459(8) Å, β = 105.2257(8)°, V = 2415.9(3) Å^3, Z = 2, μ = 1.27 mm^{-1}, 38192 reflections measured at Daresbury Laboratory Station 9.8, λ = 0.6939 Å, 5670 unique, R_{int} = 0.047, $R_1[I>2\sigma(I)]$ = 0.050, wR_2 (all data) = 0.165.

21 For **2**$^{\prime}$·H_2O: $C_{30}H_{82}N_5O_{26}S_4V_5\cdot H_2O$, M = 1311.94, monoclinic, $P2_1$, a = 13.2439(4), b = 13.3679(4), c = 31.3605(10) Å, β = 100.4436(5)°, V = 5460.2(3) Å^3, Z = 4, μ(Mo-Kα) = 1.06 mm^{-1}, λ = 0.71073 Å, 62632 reflections measured, 30874 unique, R_{int} = 0.027, $R_1[I>2\sigma(I)]$ = 0.038, wR_2 (all data) = 0.099. Disorder modelled in ethyl groups of five of the ten cations. The $HNEt_3^+$ cation at N(4) is fully disordered.

22 For **4**: $C_{102}H_{152}N_4O_{28}S_8V_2$, M = 2240.63, triclinic, $P\bar{1}$, a = 13.459(2), b = 14.920(3), c = 16.674(3) Å, α = 95.233(3), β = 111.125(3), γ = 112.613(3)°, V = 2778.6(9) Å^3, Z = 1, μ = 0.49 mm^{-1}, 82846 reflections measured at the Advanced Light Source, Berkeley, Station 11.3.1, λ = 0.7749 Å, 16757 unique, R_{int} = 0.081, $R_1[I>2\sigma(I)]$ = 0.069, wR_2 (all data) = 0.150.

23 (a) Y. Kondo, K. Endo, N. Iki, S. Miyano, F. Hamada, *J. Incl. Phenom. Macro. Chem*. 2005, **52**, 45-49. (b) N. Morohashi, F. Narumi, N. Iki, T. Hattori, S. Miyano, *Chem. Rev*. 2006, **106**, 5291-5311. (c) M. Yamada, M. R. Gandhi, U. M. R. Kunda, F. Hamada, *J. Incl. Phenom. Macro. Chem*. 2016, **85**, 1-18.

24 For **5**: $C_{108}H_{153}N_6O_{10}V$, M = 1746.29, triclinic, $P\bar{1}$, a = 16.7286(7), b = 18.2453(8), c = 18.7113(13) Å, α = 101.228(7), β = 105.150(7), γ = 105.573(7)°, V = 5090.1(5) Å^3, Z = 2, μ(Mo-Kα) = 0.156 mm^{-1}, 55764 reflections measured, λ = 0.71073 Å, 17887 unique, R_{int} = 0.075, $R_1[I>2\sigma(I)]$ = 0.086, wR_2 (all data) = 0.237.

25 C. Redshaw, M. A. Rowan, L. Warford, D. M. Homden, A. Arbaoui, M. R. J. Elsegood, S. H. Dale, T. Yamato, C. P. Casas, S. Matsui, S. Matsuura, *Chem. Eur. J*. 2007, **13**, 1090-1107.

26 For **6**: $C_{20}H_{56}N_2O_{19}V_6$, M = 934.30, monoclinic, $P2_1/n$, a = 11.3807(2), b = 10.7803(2), c = 15.5914(2) Å, β = 100.0588(10)°, V = 1883.46(5) Å^3,, Z = 2, μ(Mo-Kα) = 1.50 mm^{-1}, 16623 reflections measured, λ = 0.71073 Å, 4310 unique, R_{int} = 0.051, $R_1[I>2\sigma(I)]$ = 0.040, wR_2 (all data) = 0.089.

27 C. Daniel, H. Hartl, *J. Am. Chem. Soc*. 2009, **131,** 5101-5114.

28 Y.-R. Lu, T.-Z. Wu, C.-L. Chen, D.-H. Wei, J.-L. Chen, W.-C. Chou, C.-L. Dong, *Nano. Res. Lett.* 2015, **10**, 387, 1-6.

29 W. Rabten, M. D. Karka, T. Åkermark, H. Chen, R.-Z. Liao, F. Tinnis, J. Sun, P. E. M. Siegbahn, P. G. Andersson, B. Åkermark, *Inorg. Chem.* 2015, **54**, 4611-4620.

30 M. Okamura, M. Kondo, R. Kuga, Y. Kurashige, T. Yanai, S. Hayami, V. K. K. Praneeth, M. Yoshida, K. Yoneda, S. Kawata, S. Masaoka, *Nature* 2016, **530**, 465-468.

31 L. Tong, Y. Wang, L. Duan, Y. Xu, X. Cheng, A. Fischer, M. S. G. Ahlquist, L. Sun, *Inorg. Chem.* 2012, **51**, 3388-3398.

32 E. A. Gomaa, A. Negm, R. M. Abu-Qarn, *Measurement* 2018, **125**, 645-650.

33 H. N. Miras, R. Raptis, P. Baran, N. Lalioti, A. Harrison, T. A. Kabanos, *C. R. Chimie* 2005, **8**, 957-962.

34 (a) A. Rodriguez-Fortea, P. Alemany, S. Alvarez, E. Ruiz, E. *Eur. J. Inorg. Chem*. 2004, **1**, 143-153; (b) W. Plass, *Angew. Chem., Int. Ed. Engl*. 1996, **35,** 627-631.

35 (a) A. Arduini, A. Casnati, in Macrocycle Synthesis, Ed. D. Parker, Oxford University Press, New York, 1996, Chapter 7. (b) B. Dhawan, C. D. Gutsche, Calixarenes 10. Oxacalixarenes. *J. Org. Chem*. 1983, **48**, 1536-1539.